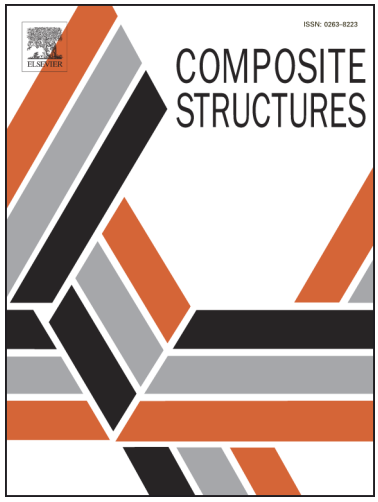

Multiple length/time-scale simulation of localized damage in composite structures using a Mesh Superposition Technique

L. Gigliotti, S.T. Pinho

PII: S0263-8223(14)00572-8
DOI: http://dx.doi.org/10.1016/j.compstruct.2014.11.005
Reference: COST 5988

To appear in: *Composite Structures*

Please cite this article as: Gigliotti, L., Pinho, S.T., Multiple length/time-scale simulation of localized damage in composite structures using a Mesh Superposition Technique, *Composite Structures* (2014), doi: http://dx.doi.org/10.1016/j.compstruct.2014.11.005

Multiple length/time-scale simulation of localized damage in composite structures using a Mesh Superposition Technique

L.Gigliotti*, S.T. Pinho

Department of Aeronautics, South Kensington Campus, Imperial College London, SW7 2AZ, London, UK

Abstract

A Mesh Superposition Technique (MST) for the progressive transition between differently-discretized subdomains is proposed and implemented in an FE code. The interfaces between these subdomains are replaced by transition regions where the corresponding meshes are superposed. The MST is applied to the multiple length/time-scale analysis of a low-velocity impact of a projectile on a composite plate. Unlike using a sudden discretization-transition approach, the use of the MST eliminates the undesirable stress disturbances at the interface between differently-discretized subdomains and, as a result, it correctly captures the impact-induced damage pattern at a lower computational cost. Finally, the MST is coupled with an implicit/explicit co-simulation technique for a multiple time/length-scale analysis. The results indicate that, if the length-scale transition is performed using the proposed MST instead of a sudden discretization-transition, the CPU time can be nearly halved.

Keywords: Composite structures, Finite element analysis (FEA), Multiple length/time-scale simulation, Damage, Mesh Superposition Technique (MST)

1. Introduction

1.1. Motivation

Numerical simulation of the mechanical response of large composite components often requires that different parts of the structure are modelled at different scales, eventually even using different physics. Multiscale modelling techniques can achieve the required level of accuracy in each part of the model while maintaining the computational time to a minimum. Within this framework, the development of suitable techniques for coupling areas of the structure discretized using different element types is crucial.

However, the coupling of subdomains discretized with finite elements of different physical dimension/formulation can introduce artificial stresses at the shared boundaries [1, 2]. Therefore, the stress field within the structure and its mechanical response may not be correctly simulated; as a result, in problems involving failure, the damage pattern might not be faithfully replicated. Additionally, in dynamic problems, the interfaces between differently-discretized subdomains may artificially reflect stress waves [3, 4].

*Corresponding author. Tel. +44(0)2075945087
Email addresses: l.gigliotti12@imperial.ac.uk (L.Gigliotti), silvestre.pinho@imperial.ac.uk (S.T. Pinho)

1.2. 3D solid elements and 2D shell elements for laminated composites

The typical finite elements used for modelling composite structures can be gathered into three categories: *(i)* three-dimensional solid elements, *(ii)* two-dimensional shell elements and *(iii)* three-dimensional shell elements.

To correctly capture the bending response, when using 3D solid elements, several elements are required through-the-thickness of the laminate, typically one per ply. Furthermore, due to their propensity to shear-locking, their aspect-ratio must be kept close to the unity. From these two considerations, it follows that models relying only on 3D solid elements are often computationally unaffordable.

Two-dimensional shell finite elements, based on Equivalent Single Layer Theories (ELST) [5, 6], represent a computationally more convenient alternative for modelling thin-walled structures. However, the simplifying assumptions of ELST are, often, too restrictive for the analysis of laminated composites (for instance, the continuity assumption made for the displacement field and its derivatives leads to continuous out-of-plane shear strains). To overcome this limitation, 2D shell elements based on Layer-wise theories [7] might be considered. For the latter, a piecewise continuous through-the-thickness displacement field is assumed and, therefore, strain-discontinuity at the plies interfaces can be modelled.

An intermediate approach between 2D shell elements and 3D solid elements is represented by the degenerated three-dimensional shell elements whose formulation is based on two-dimensional kinematic constraints [8, 9]. This type of elements represents a compromise between the computational efficiency of 2D shell elements and the modelling flexibility of 3D solid elements. Moreover, being shear-locking free, the aspect-ratio limitations of the 3D solid elements are overcome. Nonetheless, the underlying two-dimensional formulation does not provide an accurate description of the out-of-plane displacement and interlaminar stress fields, critical for delamination evaluations.

1.3. Multi-dimensional finite elements coupling

From the the previous section, it follows that 3D solid elements should be used for discretizing the area of the structure, denoted as local subdomain, where significant three-dimensional stress fields are likely to occur, e.g. indentation/impact locations and where interlaminar damage ought to be modelled. For the remaining portion of the structure, referred to as global subdomain (generally the largest portion), either 3D or 2D shell elements are preferable.

Several local/global approaches for coupling differently-discretized subdomains have been proposed, such as mixed-dimensional coupling approaches based on multi-point constraint (MPC) [1]. The MPC equations can be obtained by equating the work done by the local and global subdomains at the shared interface; a perturbation solution can be then exploited to determine the stress distribution across the thickness of the lower-dimension elements [1]. Compared to the Shell-to-Solid coupling option available in the finite element software Abaqus [10], the method is shown to eliminate the undesirable stress disturbances at the interface between differently-discretized subdomains in the case of isotropic elastic material. However, the local/global coupling must be carried at a sufficient distance from boundaries and/or discontinuities in the model [11]. In addition, the accurate derivation of the MPC equations for composite materials may become impracticable [12].

An alternative approach hinges on the use of *ad-hoc* transition elements as suggested by Dávila [2]. In this work, two transition elements have been formulated, i.e. one based on the Mindlin-Reissner [13, 14]

kinematic assumptions and a second one based on a higher-order theory similar to that developed by Tessler [15]. The stiffness matrices $\mathbf{K}_{\mathrm{Tr}}$ of the transition elements are constructed from the stiffness matrices $\mathbf{K}$ of traditional three-dimensional elements and a restraint matrix $\mathbf{R}$. Results show that, using the lower-order transition elements, it is possible to accurately model the stress fields within both the local and global models. However, within the transition elements themselves, a stress boundary layer where the interlaminar normal and shear stresses are largely overestimated, is obtained. Transition elements based on an higher-order shell theory strongly mitigate such spurious stresses [2].

Alternatively, the global and local subdomains can be coupled using an *uncoupled* global/local approach where the displacement fields computed using the global model produce the boundary conditions for the local one. The mechanical responses of the local and global models are simulated separately and the sequence of global/local analyses can be either run once (see, as an example, the Submodelling procedure implemented in Abaqus [16]) or iteratively, until the force/momentum convergence is reached at the global/local interface.

Reinoso et al. compared the Submodelling technique to Shell-to-Solid coupling [17, 18]. Here, the two approaches have been applied to the global/local FE analysis of debonding failure at the skin-stringer joint within an aeronautical component. The analysis was limited to the first stages of damage propagation, and the size of the local models was chosen to be sufficiently larger than the final expected damaged zone. As the applied load and therefore the damage area grow, stress disturbances were observed at the local/global boundaries for both approaches.

The computational advantage provided by generic global/local approaches is enhanced if the size of the three-dimensional local model is kept to a minimum. However, the transition between subdomains discretized using finite elements with different dimension/formulation should be located such that the stress field in the local subdomain has decayed to the form assumed in the formulation of the finite elements used in the global subdomain. Further, the global/local transition should be sufficiently distant from any perturbation such as boundaries or damaged zones.

The influence of the distance of the global/local transition from the delamination front was investigated by Krueger et al. for the cases of delaminated test specimens [19, 20] as well as skin/stringer debonding in an composite aircraft component [21, 22]. Results, provided in terms of the mixed-mode strain energy release rates computed using the VCCT, demonstrate that, for an acceptable agreement with the reference solution, a minimum length of which the local subdomain needs to be extended, both ahead and in the wake of delamination front, can be identified.

Bridging methods for coupling continuum models with atomistic models [23, 24], as well as discrete element models and finite element models [25–27], have been presented in the literature. In the approach described by Belytschko and Xiao [23, 24], coupled subdomains overlap at the shared interface as in the method presented here.

In this paper, we propose a new local/global coupling approach based on a Mesh Superposition Technique (MST). The interfaces between subdomains whose FE discretizations consist of different element types are replaced by transition regions where the corresponding discretizations are superposed.

The theoretical details of the MST, as well as the key aspects of its FE implementation, are presented in Section 2. The MST is applied to the multiple length/time-scales analysis of a low-velocity impact on a composite plate [28, 29] in Section 3. Results of this analysis are presented and discussed, respectively, in Section 4 and Section 5. Finally, conclusions are drawn Section 6.

2. Mesh Superposition Technique

2.1. Theory

In the literature, techniques involving superposed elements occupying the same physical space have been used to address problems in which meshing is challenging, such as in meso-scale modelling of woven composites [30–33]. In the MST we propose here, we also make use of superposed elements, albeit in a more generic way.

Let us consider a deformable body $\boldsymbol{\mathcal{B}}$ occupying the domain $\omega(t) \in \mathbb{R}^3$, where with $\mathbb{R}^3$ we denote the three-dimensional euclidean space, for any instant of time $t > 0$ (Figure 1). The domain occupied by the deformable body at instant $t = 0$ is indicated with Ω and, the position vector of each point $P \in \boldsymbol{\mathcal{B}}$ in the reference configuration is denoted as $\mathbf{X}$.

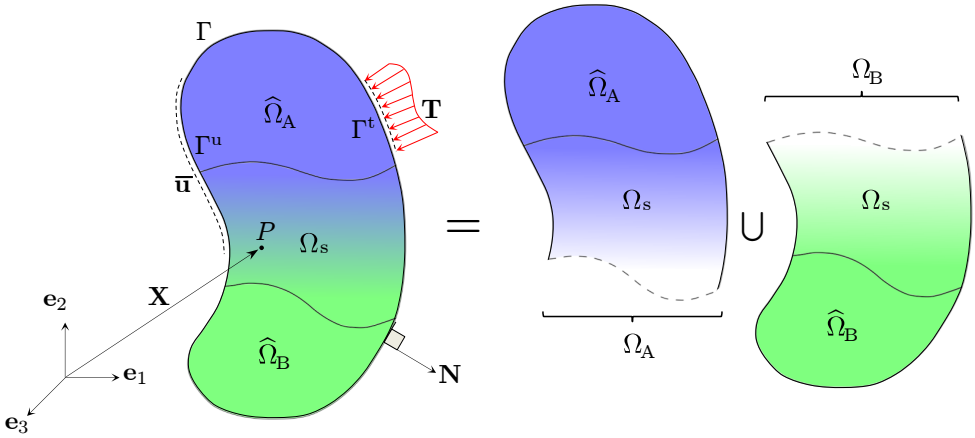

Figure 1: Mesh Superposition Technique. In the reference configuration, domain Ω is decomposed into the subdomains Ω_A and Ω_B which overlap over the subdomain Ω_s. Dirichlet and von Neumann boundary conditions are applied over specific portions of the boundary $\Gamma = \partial\Omega$.

Let the boundary of Ω be $\Gamma = \partial\Omega$, and assume that Dirichlet boundary conditions are applied over the subset $\Gamma^u \subset \Gamma$, while von Neumann boundary conditions are applied over the subset $\Gamma^t \subset \Gamma$.

We consider domain Ω to be subdivided into subdomains Ω_A and Ω_B, whose intersection is $\Omega_s \equiv \Omega_A \cap \Omega_B \neq \emptyset$. Additionally, the subdomains Ω_A and Ω_B can be conveniently decomposed, as shown in Figure 1, into an overlapping portion Ω_s and a non-overlapping one defined as

$$\widehat{\Omega}_i = \Omega_i \setminus \Omega_s \qquad \text{for} \quad i = A, B. \tag{1}$$

Let $\rho(\mathbf{X})$ and $\rho(\mathbf{X})\ddot{\mathbf{u}}(\mathbf{X},t)$ be, respectively, the material mass density and the inertia forces per unit volume. The applied body force and the Piola traction vector are denoted by $\mathbf{B}(\mathbf{X},t)$ and $\mathbf{T}(\mathbf{X},t)$ respectively. Given the applied Dirichlet and von Neumann boundary conditions, the principle of virtual work can be expressed as

$$\int_\Omega \mathbf{S} : \delta\mathbf{E}\, d\Omega + \int_\Omega \rho\ddot{\mathbf{u}} \cdot \delta\mathbf{u}\, d\Omega = \int_\Omega \mathbf{B} \cdot \delta\mathbf{u} d\Omega + \int_{\Gamma^t} \mathbf{T} \cdot \delta\mathbf{u}\, d\Gamma\,, \tag{2}$$

where $\delta\mathbf{E}(\mathbf{X},t)$ is the virtual variation of the Green-Lagrange strain tensor, and $\mathbf{S}(\mathbf{X},t)$ is the second Piola-Kirchhoff stress tensor.

Within subdomain Ω_s, where univocal definitions of the second Piola-Kirchhoff stress tensor $\mathbf{S}(\mathbf{X},t)$ and of the material density $\rho(\mathbf{X})$ do not exist, the terms of the principle of virtual work can be expressed as the linear combination of the contributions of the overlapping subdomains. These contributions are scaled by non-negative scalar-valued weighting factors $\psi_i(\mathbf{X})$, continuous over the subdomain Ω_s.

The internal virtual work δW_int, the external virtual work δW_ext and the inertial virtual work δW_kin can, therefore, be expressed as:

$$\begin{aligned}
\delta W_\mathrm{int}(\mathbf{u},\delta\mathbf{u}) &= \int_{\Omega_\mathrm{s}} \sum_{i\in\{\mathrm{A,B}\}} \left[\psi_i(\mathbf{X})\mathbf{S}_i\right] : \delta\mathbf{E}\,\mathrm{d}\Omega + \sum_{i\in\{\mathrm{A,B}\}} \left[\int_{\widehat{\Omega}_i} \mathbf{S}_i : \delta\mathbf{E}\,\mathrm{d}\Omega\right], \\
\delta W_\mathrm{ext}(\mathbf{u},\delta\mathbf{u}) &= \int_{\Omega_\mathrm{s}} \sum_{i\in\{\mathrm{A,B}\}} \left[\psi_i(\mathbf{X})\mathbf{B}_i\right] \cdot \delta\mathbf{u}\,\mathrm{d}\Omega + \sum_{i\in\{\mathrm{A,B}\}} \left[\int_{\widehat{\Omega}_i} \mathbf{B}_i \cdot \delta\mathbf{u}\,\mathrm{d}\Omega\right] + \int_{\Gamma^\mathrm{t}} \mathbf{T}\cdot\delta\mathbf{u}\,\mathrm{d}\Gamma\,, \\
\delta W_\mathrm{kin}(\mathbf{u},\delta\mathbf{u}) &= \int_{\Omega_\mathrm{s}} \sum_{i\in\{\mathrm{A,B}\}} \left[\psi_i(\mathbf{X})\rho_i\right] \ddot{\mathbf{u}}\cdot\delta\mathbf{u}\,\mathrm{d}\Omega + \sum_{i\in\{\mathrm{A,B}\}} \left[\int_{\widehat{\Omega}_i} \rho_i\ddot{\mathbf{u}}\cdot\delta\mathbf{u}\,\mathrm{d}\Omega\right],
\end{aligned} \tag{3}$$

with $\mathbf{S}_i$ and ρ_i being the second Piola-Kirchhoff stress tensors and the material mass densities of subdomains Ω_i; the applied body forces to subdomains Ω_i are denoted by $\mathbf{B}_i$.

From Equation 3 it follows that, within the subdomain Ω_s, an equivalent second Piola-Kirchhoff stress tensor $\mathbf{S}_\mathrm{s}$ and and equivalent material mass density ρ_s can be defined as

$$\mathbf{S}_\mathrm{s}(\mathbf{X},t) = \sum_{i\in\{\mathrm{A,B}\}} \psi_i(\mathbf{X})\mathbf{S}_i(\mathbf{X},t) \quad \text{and} \quad \rho_\mathrm{s}(\mathbf{X}) = \sum_{i\in\{\mathrm{A,B}\}} \psi_i(\mathbf{X})\rho_i(\mathbf{X}). \tag{4}$$

Similar considerations hold for the applied body forces $\mathbf{B}_i$. To satisfy the conservation of energy principle, the collection of weighting factors $\psi_i(\mathbf{X})$ must be a partition of unity of subdomain Ω_s, i.e.

$$\sum_{i\in\{\mathrm{A,B}\}} \psi_i(\mathbf{X}) = 1 \qquad \forall\, \mathbf{X}\in\Omega_\mathrm{s}. \tag{5}$$

2.1.1. Weighting factors computation

The weighting factors $\psi_\mathrm{A}(\mathbf{X})$ and $\psi_\mathrm{B}(\mathbf{X})$ are computed for every point $P(\mathbf{X}) : \mathbf{X}\in\Omega_\mathrm{s}$ as function of the relative distance from two generic surfaces $\mathcal{S}_\mathrm{A}$ and $\mathcal{S}_\mathrm{B}$, see Figure 2, that do not necessarily coincide with $\widehat{\Gamma}_\mathrm{A}$ and $\widehat{\Gamma}_\mathrm{B}$, i.e. the interfaces shared by Ω_s with $\widehat{\Omega}_\mathrm{A}$ and $\widehat{\Omega}_\mathrm{B}$, respectively.

The procedure to compute $\psi_\mathrm{A}(\mathbf{X})$ and $\psi_\mathrm{B}(\mathbf{X})$ consists of the following steps:

(i) Using the Level Set Method [34], evaluate the signed distances d_A and d_B of point $P(\mathbf{X})$ from surfaces $\mathcal{S}_\mathrm{A}$ and $\mathcal{S}_\mathrm{B}$. Letting the closest points to $P(\mathbf{X})$ on $\mathcal{S}_\mathrm{A}$ and $\mathcal{S}_\mathrm{B}$ be denoted, respectively, as $A(\mathbf{X}_A)$ and $B(\mathbf{X}_B)$ (see Figure 2), d_A and d_B can be expressed as

$$d_A = \|\mathbf{X}_A - \mathbf{X}\| \quad \text{and} \quad d_B = \|\mathbf{X}_B - \mathbf{X}\|\,. \tag{6}$$

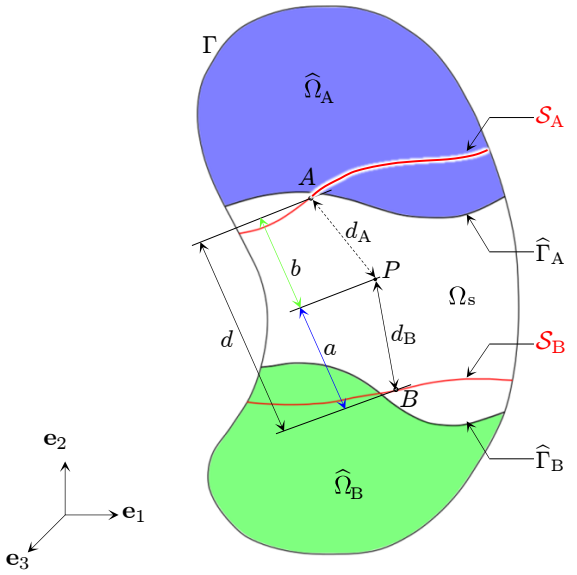

Figure 2: Distances used for the computation of the weighting factors ψ_{A} and ψ_{B}.

(ii) Compute distances d, a and b, shown in Figure 2, as

$$d = \|\mathbf{X}_B - \mathbf{X}_A\|\,,\quad a = \frac{|(\mathbf{X}_B - \mathbf{X})\cdot(\mathbf{X}_B - \mathbf{X}_A)|}{d},\quad b = \frac{|(\mathbf{X}_A - \mathbf{X})\cdot(\mathbf{X}_B - \mathbf{X}_A)|}{d} \tag{7}$$

(iii) Assign weighting factors $\psi_{\mathrm{A}}(\mathbf{X})$ and $\psi_{\mathrm{B}}(\mathbf{X})$ as:

$$\psi_A(\mathbf{X}) = \begin{cases} 0 & \Leftarrow d_A > d \\ \dfrac{a}{d} & \Leftarrow d_A, d_B < d \\ 1 & \Leftarrow d_B \geq d \end{cases} \quad \text{and} \quad \psi_B(\mathbf{X}) = \begin{cases} 0 & \Leftarrow d_B > d \\ \dfrac{b}{d} & \Leftarrow d_A, d_B < d \\ 1 & \Leftarrow d_A \geq d \end{cases} \tag{8}$$

From the definitions provided in Equations 6-8, we infer that $\psi_{\mathrm{A}}(\mathbf{X})$ and $\psi_{\mathrm{B}}(\mathbf{X})$ are continuous over Ω_{s}, and that the Partition of Unity condition (see Equation 5) is automatically satisfied.

2.2. Finite Element implementation

To derive the finite element equations associated to the problem formulated in Equation 2, let subdomains Ω_{A} and Ω_{B} be discretized with elements e^j_{A} and e^j_{B}, respectively, and let the corresponding integration domains be $\Omega_{e^j_{\mathrm{A}}}$ and $\Omega_{e^j_{\mathrm{B}}}$, such that

$$\bigcup_{e^j_{\mathrm{A}} \in \mathcal{E}_{\mathrm{A}}} \Omega_{e^j_{\mathrm{A}}} \equiv \Omega_{\mathrm{A}} \quad \text{and} \quad \bigcup_{e^j_{\mathrm{B}} \in \mathcal{E}_{\mathrm{B}}} \Omega_{e^j_{\mathrm{B}}} \equiv \Omega_{\mathrm{B}}\,, \tag{9}$$

where $\mathcal{E}_{\mathrm{A}} = \left\{ e^j_{\mathrm{A}} \right\}$ and $\mathcal{E}_{\mathrm{B}} = \left\{ e^j_{\mathrm{B}} \right\}$ indicate the sets of elements with support in subdomains Ω_{A} and Ω_{B} as shown in Figure 3.

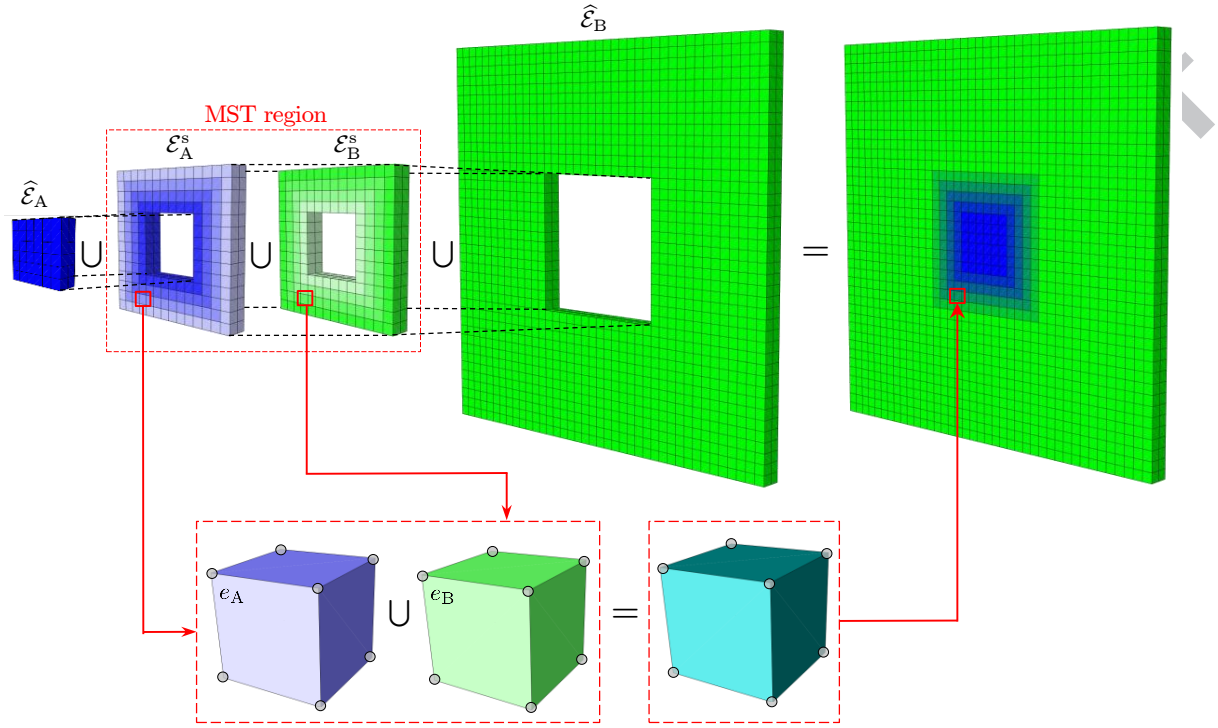

Figure 3: FE meshes of the superposed subdomains Ω_{A} and Ω_{B}. Within the MST region, the two meshes are superposed and the corresponding stiffness and mass matrices scaled, in order to satisfy the conservation of energy principle.

Proceeding as in Section 2.1, $\mathcal{E}_{\mathrm{A}}$ and $\mathcal{E}_{\mathrm{B}}$ can be further decomposed as $\mathcal{E}_{\mathrm{A}} = \widehat{\mathcal{E}}_{\mathrm{A}} \cup \mathcal{E}^{\mathrm{s}}_{\mathrm{A}}$ and $\mathcal{E}_{\mathrm{B}} = \widehat{\mathcal{E}}_{\mathrm{B}} \cup \mathcal{E}^{\mathrm{s}}_{\mathrm{B}}$, where $\widehat{\mathcal{E}}_{\mathrm{A}}$ and $\widehat{\mathcal{E}}_{\mathrm{B}}$ are the sets of elements whose support is, respectively, in subdomains $\widehat{\Omega}_{\mathrm{A}}$ and $\widehat{\Omega}_{\mathrm{B}}$. In addition, $\mathcal{E}^{\mathrm{s}}_{\mathrm{A}} \subset \mathcal{E}_{\mathrm{A}}$ and $\mathcal{E}^{\mathrm{s}}_{\mathrm{B}} \subset \mathcal{E}_{\mathrm{B}}$ denote the sets of elements which of overlap over the transition region (indicated in Figure 3 as MST region), i.e.

$$\bigcup_{e^j_{\mathrm{A}} \in \widehat{\mathcal{E}}_{\mathrm{A}}} \Omega_{e^j_{\mathrm{A}}} \equiv \widehat{\Omega}_{\mathrm{A}}\,, \qquad \bigcup_{e^j_{\mathrm{B}} \in \widehat{\mathcal{E}}_{\mathrm{B}}} \Omega_{e^j_{\mathrm{B}}} \equiv \widehat{\Omega}_{\mathrm{B}} \quad \text{and} \quad \bigcup_{e^j_{\mathrm{A}} \in \mathcal{E}^{\mathrm{s}}_{\mathrm{A}}} \Omega_{e^j_{\mathrm{A}}} \equiv \bigcup_{e^j_{\mathrm{B}} \in \mathcal{E}^{\mathrm{s}}_{\mathrm{B}}} \Omega_{e^j_{\mathrm{B}}} \equiv \Omega_{\mathrm{s}}. \tag{10}$$

From Equation 3, the stiffness matrices of elements within the MST region, i.e. $e^j_{\mathrm{A}} \in \mathcal{E}^{\mathrm{s}}_{\mathrm{A}}$ and $e^j_{\mathrm{B}} \in \mathcal{E}^{\mathrm{s}}_{\mathrm{B}}$, are given by

$$\begin{aligned} \mathbf{K}^{\mathrm{s}}_{e^j_{\mathrm{A}}} &= \int_{\Omega_{e^j_{\mathrm{A}}}} \left[\mathbf{B}^{\mathrm{T}}_{e^j_{\mathrm{A}}} \,:\, \psi_{\mathrm{A}}(\mathbf{X}) \Big(\mathbf{I} \otimes \mathbf{S}_{\mathrm{A}} + \mathbf{F} \mathbb{C}_{\mathrm{A}} \mathbf{F}^{\mathrm{T}} \Big) \,:\, \mathbf{B}_{e^j_{\mathrm{A}}} \right] \mathrm{d}\Omega_{e^j_{\mathrm{A}}} \quad \text{and} \\ \mathbf{K}^{\mathrm{s}}_{e^j_{\mathrm{B}}} &= \int_{\Omega_{e^j_{\mathrm{B}}}} \left[\mathbf{B}^{\mathrm{T}}_{e^j_{\mathrm{B}}} \,:\, \psi_{\mathrm{B}}(\mathbf{X}) \Big(\mathbf{I} \otimes \mathbf{S}_{\mathrm{B}} + \mathbf{F} \mathbb{C}_{\mathrm{B}} \mathbf{F}^{\mathrm{T}} \Big) \,:\, \mathbf{B}_{e^j_{\mathrm{B}}} \right] \mathrm{d}\Omega_{e^j_{\mathrm{B}}}\,. \end{aligned} \tag{11}$$

where $\mathbf{B}_{e^j_{\mathrm{A}}}$ and $\mathbf{B}_{e^j_{\mathrm{B}}}$ are the shape functions derivatives matrices of finite elements e^j_{A} and e^j_{B}, respectively. In addition, $\mathbb{C}_i$ is the fourth-order material elasticity tensor associated to subdomains Ω_i, $\mathbf{F}$ is the deformation gradient and $\mathbf{I}$ identifies the identity matrix.

The values of $\psi_{\mathrm{A}}(\mathbf{X})$ and $\psi_{\mathrm{B}}(\mathbf{X})$ can be assigned to each element through suitable nodal values, and the element's shape functions may be used for their evaluation at every internal point. Alternatively, if the variation of $\psi_{\mathrm{A}}(\mathbf{X})$ and $\psi_{\mathrm{B}}(\mathbf{X})$ inside each element is neglected, then the centroid value can be used to scale the constitutive properties uniformly for the entire element. Since $\psi_{\mathrm{A}}(\mathbf{X})$ and $\psi_{\mathrm{B}}(\mathbf{X})$ are computed as function of the elements' coordinates in the undeformed configuration, their values do not change as the body deforms.

Following a similar approach to the one used to define the stiffness matrices in Equation 11, the mass matrices of elements $e^j_{\mathrm{A}} \in \widehat{\mathcal{E}}_{\mathrm{A}}$ and $e^j_{\mathrm{B}} \in \widehat{\mathcal{E}}_{\mathrm{B}}$ are computed as

$$\begin{aligned} \mathbf{M}^{\mathrm{s}}_{e^j_{\mathrm{B}}} &= \int\limits_{\Omega_{e^j_{\mathrm{A}}}} \psi_{\mathrm{A}}(\mathbf{X}) \rho_{\mathrm{A}} \mathbf{N}^{\mathrm{T}}_{e^j_{\mathrm{A}}} \mathbf{N}_{e^j_{\mathrm{A}}} \, \mathrm{d}\Omega_{e^j_{\mathrm{A}}} \quad \text{and} \\ \mathbf{M}^{\mathrm{s}}_{e^j_{\mathrm{B}}} &= \int\limits_{\Omega_{e^j_{\mathrm{B}}}} \psi_{\mathrm{B}}(\mathbf{X}) \rho_{\mathrm{B}} \mathbf{N}^{\mathrm{T}}_{e^j_{\mathrm{B}}} \mathbf{N}_{e^j_{\mathrm{B}}} \, \mathrm{d}\Omega_{e^j_{\mathrm{B}}}. \end{aligned} \tag{12}$$

3. Application: Multiple length/time-scale analysis of low-velocity impact on a composite plate

3.1. Problem description

The MST is applied for simulating the low-velocity impact response of $[0^\circ_3/90^\circ_3]_{\mathrm{s}}$ cross-ply laminates made of HS160/REM graphite/epoxy [28, 29]. The specimens were rectangular with a 65.0 mm × 87.5 mm in-plane area and a nominal thickness h of 2.0 mm. The specimens were impacted with a 2.3 kg hemispherical impactor 12.5 mm in diameter and were simply supported on a steel plate with a rectangular (45.0 mm × 67.5 mm) opening.

An impact energy of 3.1 J was used in the experiments [28, 29]; the impact-induced damage consists of an initial tensile matrix crack in the distal 0° layers, followed by a two-lobe shaped delamination at the bottom 0°/90° interface as shown in Figure 4.

3.2. Finite Element models

Composite structures subjected to low-velocity impact of small objects experience localized damage confined within the area surrounding the impact location [35]. Therefore, to accurately simulate such localized damage, while maintaining the required computational cost to a minimum, different parts of the structure need to be modelled at different lenght-scales. More precisely, the area surrounding the impact location can be conveniently modelled at the meso-scale while the remaining of the structure being modelled at the macro-scale [36]. In the following, we will refer to the area modelled at the meso-scale, either as *meso-scale region* or *local region*, as opposed to the remaining area, referred to as the *macro-scale region* or *global region*. The in-plane area of the meso-scale region will be denoted as $A_{\mathrm{meso}} = L_{\mathrm{meso}} \times W_{\mathrm{meso}}$ while, $A_{\mathrm{tot}} = L \times W$ is the panel's in-plane area, see Figure 5a. In the work presented here, the panel's in-plane area A_{tot} was kept constant, while the width W_{meso} and the length L_{meso} of the meso-scale region were varied.

Within the meso-scale region, the differently-oriented sublaminates are individually modelled, as well as the interfaces between them. To correctly capture the three-dimensional stress field at the impact location,

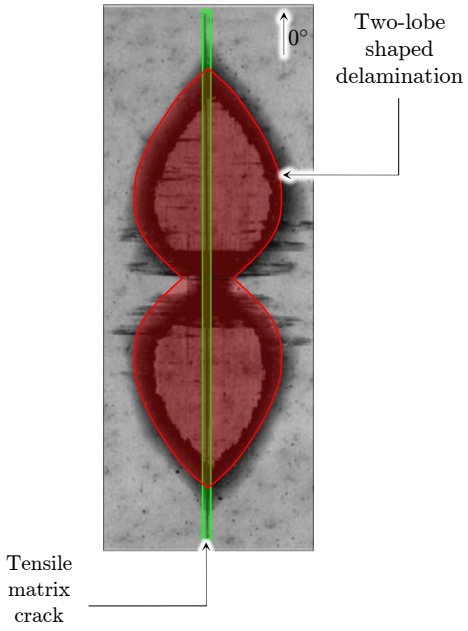

Figure 4: Impact-induced damage pattern on $[0_3^\circ/90_3^\circ]_s$ laminate. X-rays analysis shows that the main failure modes are represented by a tensile matrix cracking of the distal 0_3° sublaminate (green) and by a two-lobe shaped delamination at the bottom $0^\circ/90^\circ$ interface (red), after [29].

3D solid elements are used in this region. The remaining of the structure, modelled at the macro-scale, is conveniently discretized using either 3D or conventional 2D shell elements.

FE models of the impacted composite plates were built using the finite elements software Abaqus (6.12-1) [16], through the in-built Python scripting facilities [37]. Because of the symmetry, only one quarter of the specimen was modelled and only the portion of the specimen within the rectangular opening was considered, as schematically shown in Figure 5a. The impactor's deformations were assumed negligibly small and, therefore, it was modelled using rigid surface elements (R3D4); the impactor-plate contact interaction was simulated by surface-to-surface contact elements between the impactor surface and the top surface of the plate.

The reference solution of the problem in Section 3.1 was obtained with a fully local model, denoted as `FL` model and shown in Figure 5b. Here, the plies are uniformly discretized using eight-noded reduced-integration solid elements (C3D8R) and cohesive elements were inserted at the bottom $0^\circ/90^\circ$ interface over the entire plate's in-plane area A_{tot}.

The MST was applied for both a 3D/3D coupling and a 3D/2D coupling. In total, four multi-scale models were built: *(i)* two models with a sudden discretization-transition between the meso-scale and the macro-scale region, denoted as 3D/3D `ST` (Figure 6a) and 3D/2D `ST` (Figure 7a) and *(ii)* two models where the sudden discretization-transition of the ST models is replaced by a transition region over which the discretizations are superposed, and referred to as 3D/3D `MST` (Figure 6b) and 3D/2D `MST` (Figure 7b). A constant width of four elements in the laminate's plane was considered for the MST region.

To model interlaminar failure, a layer of cohesive elements (COH3D8) was inserted at the bottom $0^\circ/90^\circ$

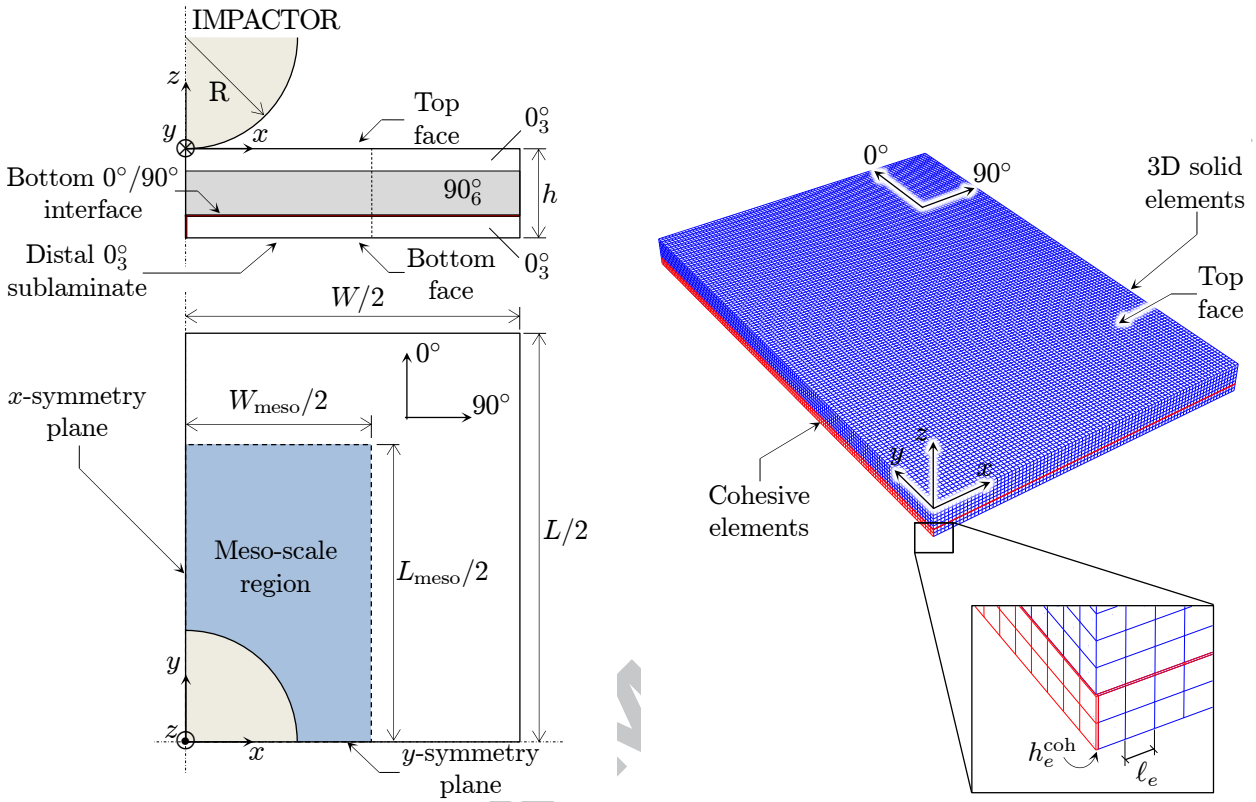

(a) Schematic (not in scale) with layup and dimensions of plate and impactor.

(b) `FL` model.

Figure 5: Schematic of the impacted specimens with definition of the meso-scale region (**a**) and the `FL` model used to obtain the reference solution (**b**).

interface while two rows of cohesive elements, placed at the symmetry plane parallel to the 0°-plies direction, were used to simulate tensile matrix cracking (see Figures 5b-7b). A mixed-mode bilinear traction-separation law was used to simulate the softening and fracture response [38, 39]. A quadratic stress-based criterion and a linear energy-based criterion were assumed, respectively, for damage initiation and propagation.

The material properties used by Aymerich et al. [28] in their simulations are shown in Table 1. Although they did not use the typical assumption of transverse isotropy, we used the same properties in our simulations so that meaningful comparison can be drawn. The cohesive properties of the interfaces were calibrated against experimental data from static Mode I (DCB) and Mode II (ENF) fracture tests on unidirectional laminates [28].

3.2.1. Multiple length-scale analysis

Within the meso-scale region (see Figure 5a), composite plies were discretized using eight-noded reduced-integration solid elements (C3D8R) and delamination initiation/propagation at the bottom 0°/90° interface was taken into account using cohesive elements. Within the macro-scale region, for the 3D/3D models, eight-noded reduced integration 3D shell elements (SC8R) were used; the latter were replaced by conventional four-noded reduced-integration 2D shell elements for the 3D/2D models. Both 3D and 2D shell elements

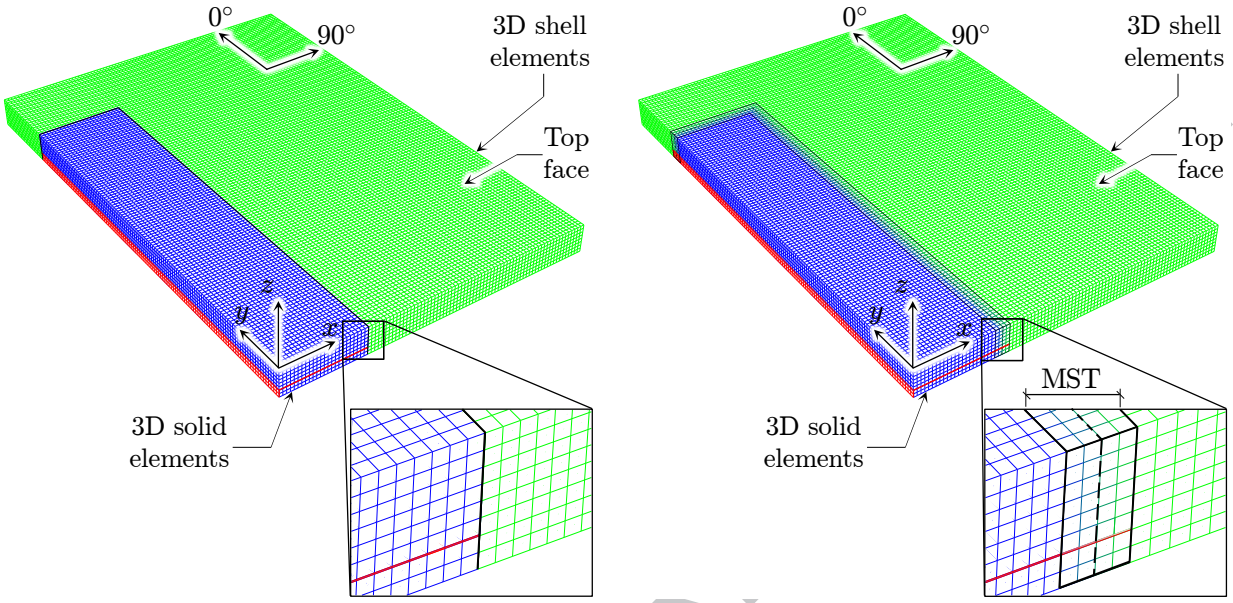

(a) 3D/3D `ST` model. **(b)** 3D/3D `MST` model.

Figure 6: `ST` and `MST` models used for the 3D/3D meso/macro coupling. 3D solid elements and 3D shell elements are displayed, respectively, in blue and green, while the cohesive elements are shown in red.

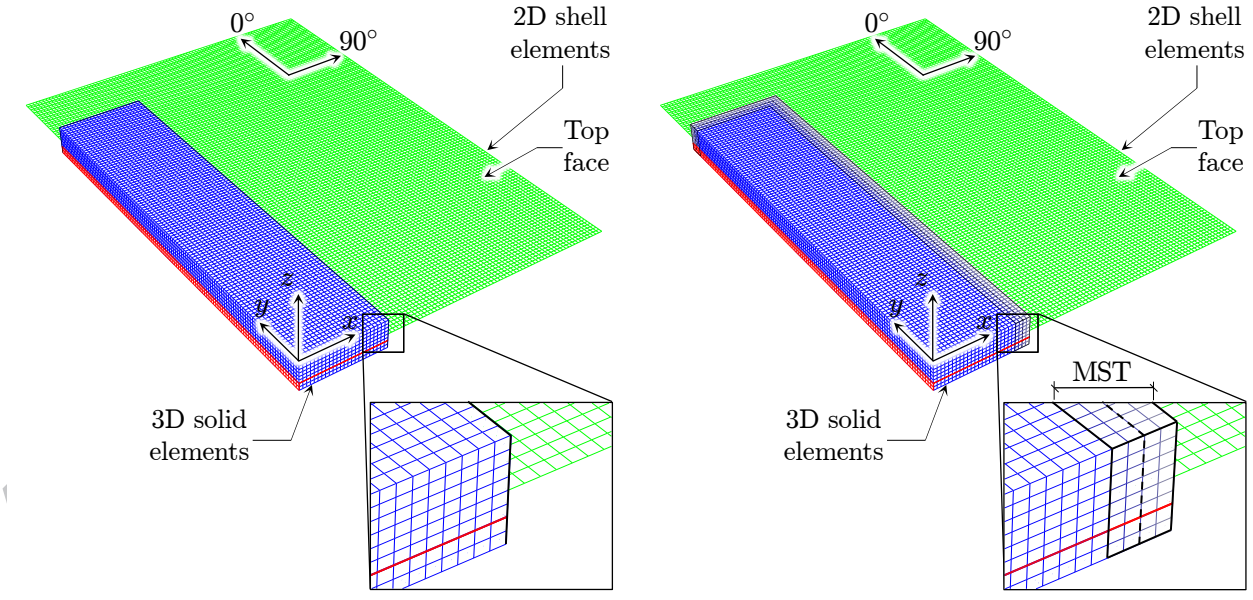

(a) 3D/2D `ST` model. **(b)** 3D/2D `MST` model.

Figure 7: `ST` and `MST` models used for the 3D/2D meso/macro coupling. 3D solid elements and conventional 2D shell elements are displayed, respectively, in blue and green, while the cohesive elements are shown in red.

Table 1: Elastic properties of the plies, cohesive properties of the interfaces, and density used by Aymerich et al. [28].

E_{11}	$E_{22}=E_{33}$	$G_{12}=G_{13}=G_{23}$	$\nu_{12}=\nu_{13}=\nu_{23}$	ρ
93.7 GPa	7.45 GPa	3.97 GPa	0.261	1600 kg/m^3
k_N		N	G_{Ic}	
120 GPa/mm		30 MPa	520 J/m^2	
$k_S=k_T$		$S=T$	$G_{\mathrm{IIc}}=G_{\mathrm{IIIc}}$	
43 GPa/mm		80 MPa	970 J/m^2	

were not integrated though-the-thickness during the analysis; therefore, no additional integration points were needed.

For all models, a constant in-plane element length $\ell_e = 0.25\,\mathrm{mm}$ was adopted for the entire structure and, a thickness $h_e^{\mathrm{coh}} = 20\,\mu\mathrm{m}$ was used for the cohesive elements. Each of the 0°_3 and 90°_3 sublaminates were discretized with two elements through their thickness when three-dimensional (solid or shell) elements were used.

Simply supported boundary conditions were enforced either by constraining the z-displacement of the nodes initially lying on the edges of rectangular supporting opening (3D/3D models), or through specific MPC equations prescribed at the shell elements' nodes on the outer edges of the panel (3D/2D models). Further MPC equations were prescribed at the shell-to-solid interfaces including, for the 3D/2D `MST` model, the nodes within the MST regions.

Simulations were performed using Abaqus/Explicit with a constant time step $\Delta t = 10\,\mathrm{ns}$ ($\Delta t_{\mathrm{stable}} \approx 16.22\,\mathrm{ns}$) and the total analysis time was equal to 4 ms. No mass scaling was considered during the simulations and enhanced hourglass control was used for reduced-integration elements.

3.2.2. Multiple length and time-scale analysis

In addition to the multiple length-scale approach introduced in Section 3.2.1, a multi-solver technique can be exploited. In the latter, different solvers can be used to simulate the mechanical response of different portions of the structure, depending on where they are expected to provide the most computationally efficient solution. Considering the problem in Section 3.1, material failure and complex contact interactions at the impact location are best analysed using FE solvers based on explicit time-integration schemes, e.g. Abaqus/Explicit, while the elastic behaviour of light and stiff components can, more efficiently, be simulated with FE solvers using implicit time-integration schemes, e.g. Abaqus/Standard.

The use of different solvers leads to the definition of multiple time-scales at which the structural response is simulated, i.e. an explicit/micro time-scale and an implicit/macro time-scale. The former is characterized by a high number of short and relatively inexpensive time-steps, while a reduced number of larger time-steps are required when implicit integrators are used, due to their unconditional stability.

Within this framework, the 3D/2D `ST` and `MST` models were decomposed into an explicit and an implicit sub-model as shown in Figure 8. The 3D/2D coupling, either using a sudden discretization-transition (Figure 8a) or the proposed MST (Figure 8b), is carried out within the explicit sub-model.

Simulations were performed using Abaqus/Explicit for the explicit sub-model with a constant time-step $\Delta t_{\mathrm{Xpl}} = 10\,\mathrm{ns}$ ($\Delta t_{\mathrm{stable}} \approx 16.22\,\mathrm{ns}$) while Abaqus/Standard was used for the implicit sub-model, with a constant time-step of $\Delta t_{\mathrm{Imp}} = 1\,\mathrm{ms}$; the total analysis time was also equal to 4 ms. Enhanced hourglass control was considered for reduced-integration elements and no mass scaling was used within Abaqus/Explicit.

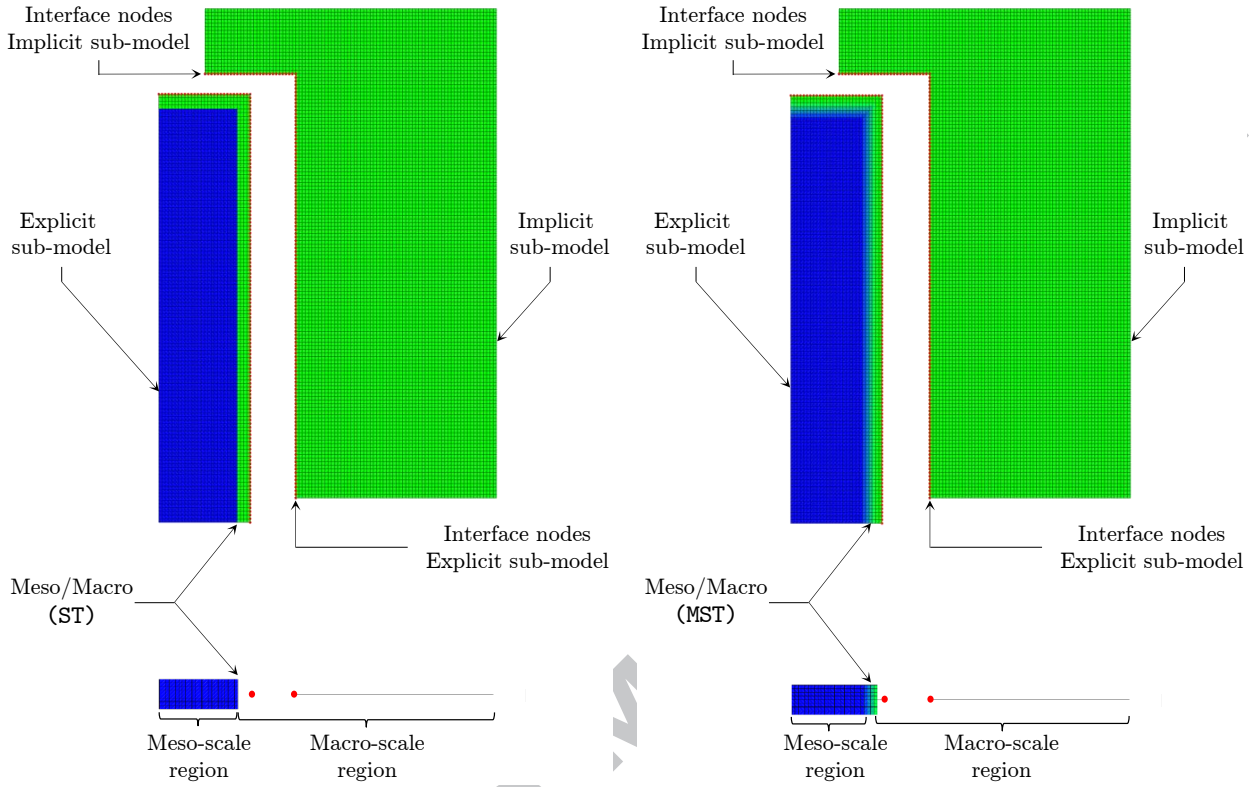

(a) `ST` multi time/length-scale model. **(b)** `MST` multi time/length-scale model.

Figure 8: Multiple length/time-scale models. The 3D/2D ST and MST models are decomposed into an explicit and an implicit sub-model which interact through the interface nodes displayed in red.

The explicit and implicit analyses are coupled using the GC method [40, 41], a staggered method built within the framework of the FETI method [42, 43] and implemented in Abaqus [16] in the form of a Co-Simulation Engine (CSE). The velocity continuity is prescribed at the interface nodes (displayed in red[1] in Figure 8) by means of Lagrange multipliers. Although the detailed description of the GC method is beyond the purpose of this paper, it is worth noting that its computational efficiency is primarily dependent on the number of degrees of freedom (DOFs) belonging to the explicit sub-model and on the number of interface nodes.

4. Results

4.1. Damage prediction

The interlaminar damage pattern at the bottom $0°/90°$ interface, simulated with the FE models detailed in Section 3.2.1, and using $A_{\text{meso}} = 28.25 \times 6.00\,\text{mm}^2$, is shown for $t = 2.0\,\text{ms}$ and $t = 4.0\,\text{ms}$, in Figure 9a and Figure 9b, respectively.

[1]For interpretation of the references to colors, the reader is referred to the web version of this article.

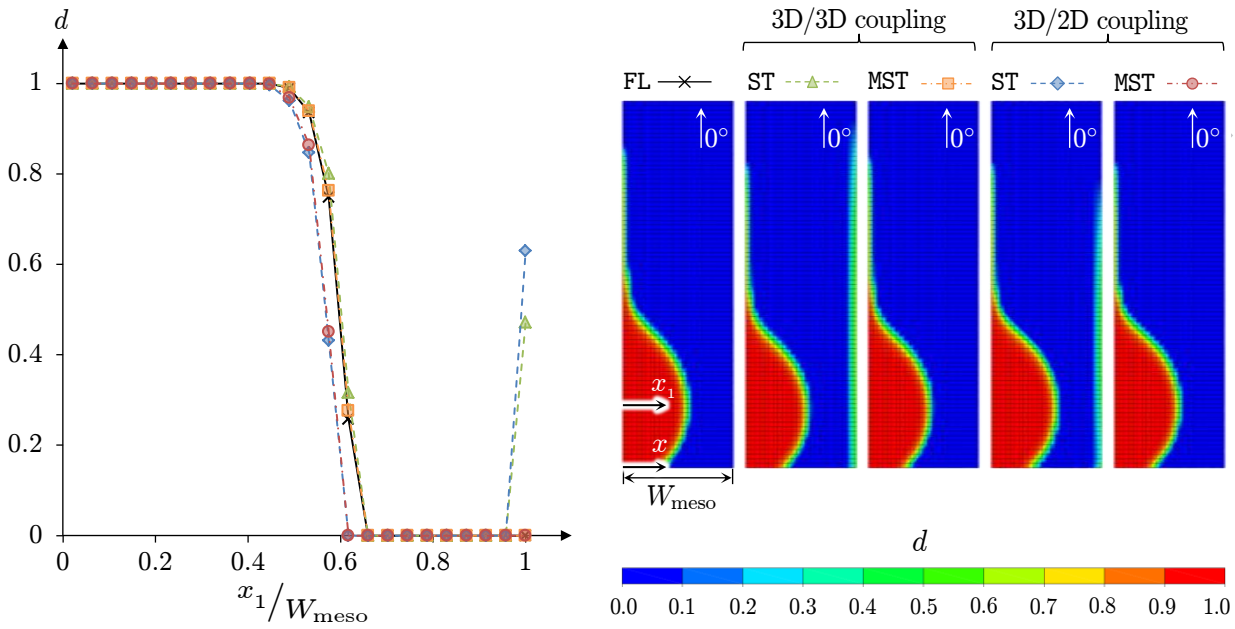

(a) $t = 2.0$ ms.

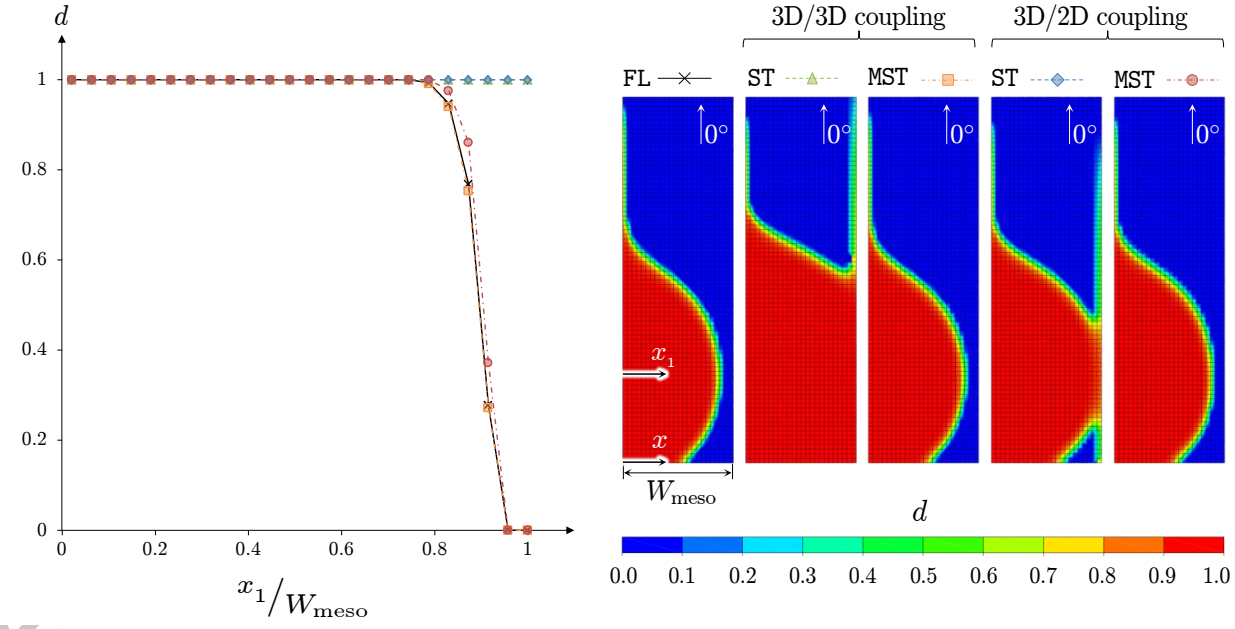

(b) $t = 4.0$ ms.

Figure 9: Interlaminar damage evolution at the bottom 0°/90° interface. On the left, the evolution of the damage variable d as function of the horizontal distance from the impact location; the x_1-coordinate corresponds to the height where the delamination attains its maximum extension (3.375 mm for **(a)** and 4.875 mm for **(b)**). On the right, the delamination pattern for the five FE models considered.

4.2. Computational efficiency

4.2.1. Multiple length-scale analysis

The CPU time $\mathfrak{t}$ associated to the 3D/2D ST and to the 3D/2D MST models as function of the normalized meso-scale area $\frac{A_{\text{meso}}}{A_{\text{tot}}}$, is provided in Figure 10a. Results are normalized with respect to the CPU time of the FL model $\mathfrak{t}^{[\text{FL}]}$.

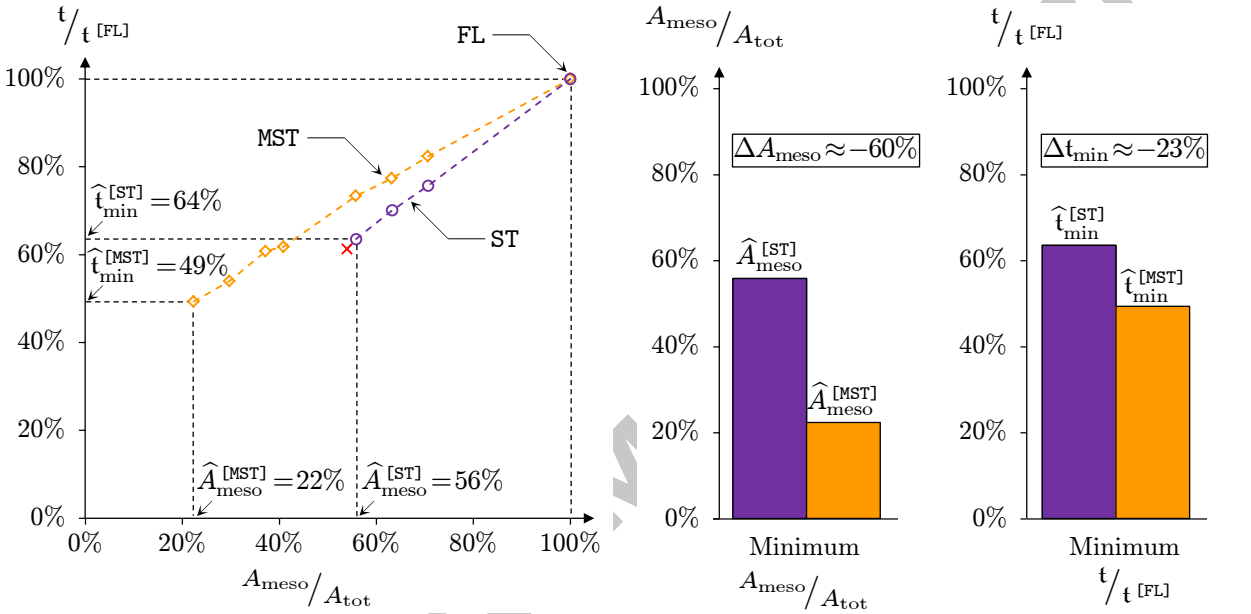

(a) Normalized CPU time as function of the normalized meso-scale area for the 3D/2D ST and MST models. The extension of the meso-scale region is progressively reduced and the data point indicated with the red cross represents the first configuration for which artificial damage at the discretization-transition is observed.

(b) On the left, the comparison between the smallest meso-scale areas required to correctly capture the damage pattern, with the ST model and the MST model; on the right, the comparison between the corresponding CPU times required by the optimal ST and the optimal MST model.

Figure 10: Computational efficiency of the MST. The MST models allow the use of smaller meso-scale areas and, thus, lower CPU times. For the proposed example, using the MST the meso-scale area is reduced by nearly 60%, while the CPU time by nearly 23%.

Starting from the reference configuration (FL model), the extension of the meso-scale region was progressively reduced until interlaminar damage was observed at the meso/macro-scale interface. The minimum meso-scale areas required to correctly replicate the damage pattern when using either the ST or the MST model, denoted in Figure 10a respectively as $\widehat{A}^{[\text{ST}]}_{\text{meso}}$ and $\widehat{A}^{[\text{MST}]}_{\text{meso}}$, are compared in Figure 10b, together with the corresponding CPU times $\widehat{\mathfrak{t}}^{[\text{ST}]}_{\text{min}}$ and $\widehat{\mathfrak{t}}^{[\text{MST}]}_{\text{min}}$. Additionally, in Figure 10b we evaluated the benefits of the MST through the reduction of meso-scale area ΔA_{meso} and the resulting reduction of CPU time $\Delta \mathfrak{t}_{\text{min}}$ achieved when using the MST instead of a sudden discretization-transition as:

$$\Delta A_{\text{meso}} = \frac{\widehat{A}^{[\text{MST}]}_{\text{meso}} - \widehat{A}^{[\text{ST}]}_{\text{meso}}}{\widehat{A}^{[\text{ST}]}_{\text{meso}}} \quad \text{and} \quad \Delta \mathfrak{t}_{\text{min}} = \frac{\widehat{\mathfrak{t}}^{[\text{MST}]}_{\text{min}} - \widehat{\mathfrak{t}}^{[\text{ST}]}_{\text{min}}}{\widehat{\mathfrak{t}}^{[\text{ST}]}_{\text{min}}} \,. \tag{13}$$

4.2.2. Multiple length/time-scale analysis

The ST and MST models used for the multiple length/time-scale analysis have, respectively, a meso-scale area equal to $\widehat{A}_{\text{meso}}^{[\text{ST}]}$ and to $\widehat{A}_{\text{meso}}^{[\text{MST}]}$, i.e. the smallest meso-scale areas for which damage is correctly replicated with the sudden-discretization transition approach and using the proposed MST, respectively. The number of DOFs in the explicit sub-model and the number of interface nodes for the ST model and for the MST model are compared, respectively, in Figures 11a and 11b.

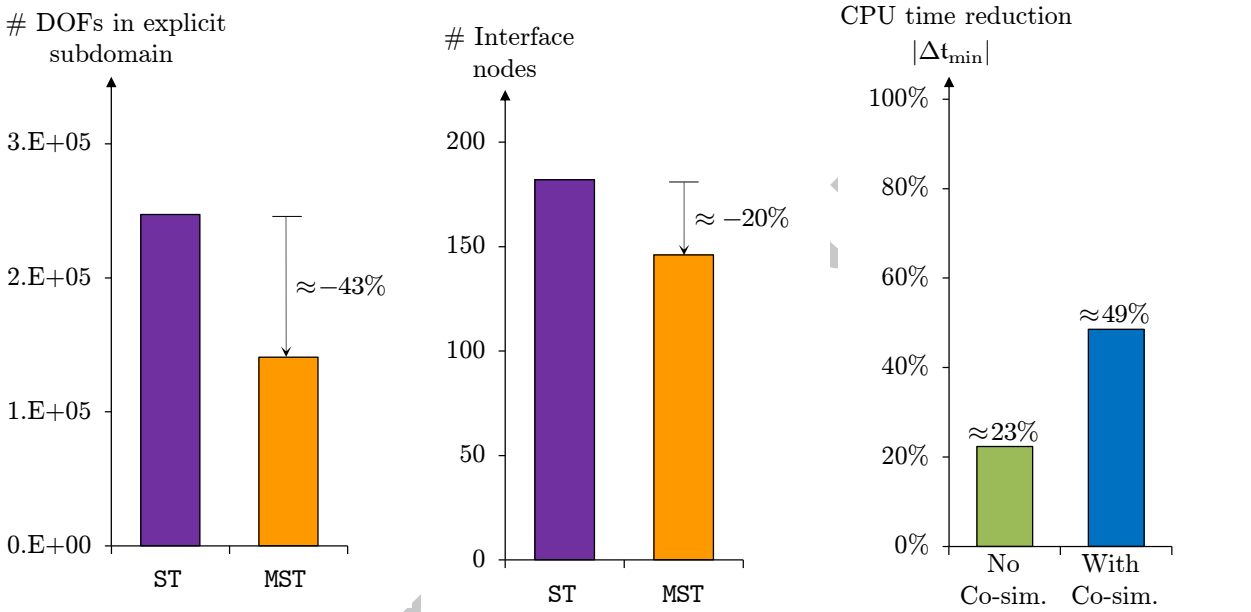

(a) Number of DOFs in the explicit sub-model.

(b) Number of interface nodes.

(c) CPU time reduction when using the MST.

Figure 11: Computational efficiency of the MST model coupled with an implicit/explicit co-simulation technique.

In Figure 11c, the absolute CPU time reductions $|\Delta t_{\text{min}}|$ achievable with the MST are compared for the cases of multiple length-scale analysis and of multiple length/time-scale analysis.

5. Discussion

5.1. Multiple length-scale analysis

The stress field disturbances resulting from the local/global coupling can lead to unrealistic interlaminar failure at the meso/macro-scale interface, particularly when a sudden discretization-transition approach is adopted (ST models), see Figure 9.

From the evolution of the damage variable d at $t = 2.0\,\text{ms}$ (Figure 9a), it follows that, the stress disturbances are more pronounced in the case of 3D/2D coupling rather than for the 3D/3D case. Moreover, when compared to the 3D/3D models, the extension of the lobe-shaped delamination is slightly underestimated when using the 3D/2D models (Figure 9a). This characteristic is probably related to the different bending response of 3D solid elements and 2D shell elements.

If the discretization-transition is sufficiently close to the impact location, as the two lobe shaped delamination grows, the latter interacts with the artificial failure at the discretization-transition, resulting in excessively large delamination areas (see Figure 9b). The delaminated area predicted with the 3D/3D `ST` model is much larger than that obtained using the 3D/2D `ST` model.

The CPU time associated to the `ST` and `MST` models decreases linearly with the extension of the meso-scale region (see Figure 10a) and, as a result of the higher number of elements and of MPC equations required at the global/local coupling, for equal values of A_{meso} the CPU time associated to the `ST` models is always lower than that of the `MST` models. However, as the distance of the discretization-transition from the impact location decreases, the damage pattern is not correctly replicated and failure at the global/local interface is simulated when using the `ST` models. In Figure 10a, the first configuration for which the delamination pattern is not correctly predicted with the `ST` models is marked with a red cross. With the proposed MST, it is possible to use smaller meso-scale regions ($\Delta A_{\text{meso}} \approx -60\%$) while accurately modelling the damage pattern, as well as lower CPU times ($\Delta \mathrm{t}_{\text{min}} \approx -23\%$) as shown in Figure 10b.

Although these specific values are, admittedly, dependent on the model's size and on the specific analysis performed, they confirm the capabilities of the approach proposed in this paper. The apparently large discrepancy between the reduction of the meso-scale area and the corresponding computational gain (60% v.s 23%) is justifiable by the higher number of finite elements and of MPC equations required when using the MST.

5.1.1. Multiple length/time-scale analysis

The GC co-simulation technique has been successfully applied to study the response of reinforced concrete structures subjected blast [44] and earthquake loading [45]. Additional applications include the simulation of tire/road interaction during full vehicle durability tests [46, 47]. Recently, Brun et al. [48] analysed a flat composite stiffened panel subjected to localised loads. In Brun et al.'s work [48], damage was not modelled and the time-scale transition was not combined with an effective coupling between different length scales.

To the best of the authors' knowledge, the example proposed in this paper represents the first attempt towards the multiple length/time-scale modelling of composite structures experiencing localized damage.

When the MST is combined with the implicit/explicit co-simulation for a multiple length/time-scale analysis, the possibility to minimize the meso-scale area becomes even more attractive. Interestingly, within the framework of a multiple length/time-scale analysis, the meso-scale area reduction provided by the MST, as opposed to a sudden discretization-transition approach, allows to decrease of the number of DOFs in the explicit sub-model and of interfaces nodes, by about 43% and 20%, respectively (see Figures 11a and 11b). As a result, the CPU time reduction achieved when using the MST increases, from the 23% obtained for the multiple length-scale analysis, to about 49% in the case of multiple length/time-scale analysis.

6. Conclusions

In this paper, a Mesh Superposition Technique (MST) for a progressive element-type transition between differently-discretized subdomains is proposed.

The MST is applied to the multiple length/time-scale analysis of a composite plate subjected to low-velocity impact. The area of the structure that, in order to correctly capture the damage pattern, needs to be modelled at the smallest length-scale can be significantly reduced when compared to a local/global

model with a sudden discretization-transition (approximately 60% for the proposed example) and, therefore, a computational cost saving might be achieved (approximately 23% CPU time reduction).

Finally, the MST was coupled with an implicit/explicit co-simulation technique for a multiple time/length-scale analysis. The results indicate that, if the length-scale transition is performed using the proposed MST instead of a sudden discretization-transition, the CPU time can be approximately halved (49%).

7. Acknowledgements

The funding from Airbus Operations Ltd (UK) is gratefully acknowledged.

References

[1] R.W. McCune and C.G. Armstrong and D.J. Robinson, Mixed-dimensional coupling in finite element models, Int. J. Numer. Methods Eng. 49 (6) (2000) 725–750.
[2] C.G. Dávila, Solid-to-shell transition elements for the computation of interlaminar stresses, Comput. Syst. Eng. 5 (2) (1994) 193–202.
[3] Z.P. Bažant, Spurious reflection of elastic waves in nonuniform finite element grids, Comput. Methods Appl. Mech. Eng. 16 (1) (1978) 91–100.
[4] Z. Celep and D. Turhan, Transient wave propagation in constant and linear strain finite elements, J. Sound Vib. 116 (1) (1987) 15–23.
[5] J.N. Reddy, Mechanics of laminated composite plates and shells: theory and analysis, CRC press, 2004.
[6] I. Kreja, A literature review on computational models for laminated composite and sandwich panels, Cent. Eur. J. Eng. 1 (1) (2011) 59–80.
[7] J.N. Reddy, An evaluation of equivalent-single-layer and layerwise theories of composite laminates, Compos. Struct. 25 (1) (1993) 21–35.
[8] W.C. Chao and N.J. Reddy, Analysis of laminated composite shells using a degenerated 3-D element, Int. J. Numer. Methods Eng. 20 (11) (1984) 1991–2007.
[9] E.J. Barbero, A 3-D finite element for laminated composites with 2-D kinematic constraints, Comput. & Struct. 45 (2) (1992) 263–271.
[10] Dassault Systémes Simulia Corp., ABAQUS 6.12 Theory Manual, 2012.
[11] K. Shim, D. Monaghan, C. Armstrong, Mixed dimensional coupling in finite element stress analysis, Eng. Comput. 18 (3) (2002) 241–252.
[12] N. Osawa and K. Hashimoto and J. Sawamura and T. Nakai and S. Suzuki, Study on shell-solid coupling FE analysis for fatigue assessment of ship structure, Mar. Struct. 20 (3) (2007) 143–163.
[13] R.D. Mindlin, Influence of rotary inertia and shear on flexural motions of isotropic, elastic plates, J. Appl. Mech. 18 (1951) 31–38.
[14] E. Reissner, The effect of transverse shear deformation on the bending of elastic plates, J. Appl. Mech. 12 (1945) 69–77.
[15] A. Tessler, A higher-order plate theory with ideal finite element suitability, Comput. Methods Appl. Mech. Eng. 85 (2) (1991) 183–205.
[16] Dassault Systémes Simulia Corp., ABAQUS 6.12 User's Manual, 2012.
[17] J. Reinoso and A. Blázquez and A. Estefani and F. París and J. Cañas and E. Arévalo and F. Cruz, Experimental and three-dimensional global-local finite element analysis of a composite component including degradation process at the interfaces, Compos. Part B 43 (4) (2012) 1929–1942.
[18] J. Reinoso and A. Blazquez and A. Estefani and F. Paris and J. Canas, A composite runout specimen subjected to tension–compression loading conditions: Experimental and global–local finite element analysis, Compos. Struct. 101 (2013) 274–289.
[19] R.Krueger and T.K. O'Brien, A shell/3D modeling technique for the analysis of delaminated composite laminates, Compos. Part A 32 (1) (2001) 25–44.
[20] R.Krueger and J. Ratcliffe and P.J. Minguet, Analysis of composite panel-stiffener debonding using a shell/3D modeling technique, NASA/CR-2007-214879 NIA Report No. 2007-07.
[21] R. Krueger and P.J. Minguet, Analysis of composite skin-stiffener debond specimens using a shell/3D modeling technique, Compos. Struct. 81 (1) (2007) 41–59.
[22] R. Krueger and J.C. Ratcliffe and P.J. Minguet, Panel stiffener debonding analysis using a shell/3D modeling technique, Compos. Sci. Tech. 69 (14) (2009) 2352–2362.
[23] T. Belytschko and S.P. Xiao, Coupling methods for continuum model with molecular model, Int. J. Multiscale Comput. Eng. 1 (1) (2003) 115–126.
[24] S.P. Xiao and T. Belytschko, A bridging domain method for coupling continua with molecular dynamics, Comput. Methods Appl. Mech. Eng. 193 (17) (2004) 1645–1669.
[25] N. Bićanić, Discrete Element Methods, John Wiley & Sons (Ltd), 2004.

[26] J. Rojek and E. Oñate, Multiscale analysis using a coupled discrete/finite element model, Interact. Multiscale Mech. 1 (1) (2007) 1–31.
[27] Y. Lee and C. Basaran, A multiscale modeling technique for bridging molecular dynamics with finite element method, J. Comput. Phys. 253 (2013) 64–85.
[28] F. Aymerich and C. Pani and P. Priolo, Damage response of stitched cross-ply laminates under impact loadings, Eng. Fract. Mech. 74 (4) (2007) 500–514.
[29] F. Aymerich and F. Dore and P. Priolo, Prediction of impact-induced delamination in cross-ply composite laminates using cohesive interface elements, Compos. Sci. Tech. 68 (12) (2008) 2383–2390.
[30] W-G. Jiang and S.R. Hallett and M.R. Wisnom, Development of domain superposition technique for the modelling of woven fabric composites, in: Mech. response of compos., Springer, 2008, pp. 281–291.
[31] E.V. Iarve and D.H. Mollenhauer and E.G. Zhou and T. Breitzman and T.J. Whitney, Independent mesh method-based prediction of local and volume average fields in textile composites, Compos. Part A 40 (12) (2009) 1880–1890.
[32] S.A. Tabatabaei and S.V. Lomov and I. Verpoest, Assessment of embedded element technique in meso-FE modelling of fibre reinforced composites, Compos. Struct. 107 (0) (2014) 436–446.
[33] S.V. Lomov and D.S. Ivanov and I. Verpoest and M. Zako and T. Kurashiki and H. Nakai and S. Hirosawa, Meso-FE modelling of textile composites: Road map, data flow and algorithms, Compos. Sci. Tech. 67 (9) (2007) 1870–1891.
[34] S. Osher and J.A. Sethian, Fronts propagating with curvature-dependent speed: algorithms based on Hamilton-Jacobi formulations, J. Comput. Phys. 79 (1) (1988) 12–49.
[35] S. Abrate, Impact on composite structures, Cambridge University Press, 2005.
[36] J. LLorca and C. González and J.M. Molina-Aldareguía and J. Segurado and R. Seltzer and F. Sket and M. Rodríguez and S. Sádaba and R. Muñoz and L.P. Canal, Multiscale modeling of composite materials: a roadmap towards virtual testing, Adv. Mater. 23 (44) (2011) 5130–5147.
[37] Dassault Systémes Simulia Corp., ABAQUS 6.12 Scripting Reference Manual, 2012.
[38] G. Alfano and M.A. Crisfield, Finite element interface models for the delamination analysis of laminated composites: mechanical and computational issues, Int. J. Numer. Methods in Eng. 50 (7) (2001) 1701–1736.
[39] Q. Yang and B. Cox, Cohesive models for damage evolution in laminated composites, Int. J. Fract. 133 (2) (2005) 107–137.
[40] A. Gravouil, A. Combescure, Multi-time-step explicit–implicit method for non-linear structural dynamics, Int. J. Numer. Methods in Eng. 50 (1) (2001) 199–225.
[41] A. Combescure and A. Gravouil, A numerical scheme to couple subdomains with different time-steps for predominantly linear transient analysis, Comput. Methods Appl. Mech. Eng. 191 (11) (2002) 1129–1157.
[42] C. Farhat and F.X. Roux, A method of finite element tearing and interconnecting and its parallel solution algorithm, Int. J. Numer. Methods Eng. 32 (6) (1991) 1205–1227.
[43] C. Farhat and K. Pierson and M. Lesoinne, The second generation FETI methods and their application to the parallel solution of large-scale linear and geometrically non-linear structural analysis problems, Comput. Methods Appl. Mech. Eng. 184 (2-4).
[44] M. Brun and A. Batti and A. Limam and A. Gravouil, Explicit/implicit multi-time step co-computations for blast analyses on a reinforced concrete frame structure, Finite Elem. Anal. Des. 52 (2012) 41–59.
[45] M. Brun and A. Batti and A. Limam and A. Combescure, Implicit/explicit multi-time step co-computations for predicting reinforced concrete structure response under earthquake loading, Soil Dyn. Earthq. Eng. 33 (1) (2012) 19–37.
[46] E. Duni and G. Toniato and R. Saponaro and P. Smeriglio and V. Puleo, Vehicle dynamic solution based on finite element tire/road interaction implemented through Implicit/Explicit sequential and Co-Simulation approach (SAE Technical Paper 2010-01-1138).
[47] H. Surendranath and V. Oancea and S. Subbarayalu, Full vehicle durability prediction using Co-Simulation between Implicit and Explicit finite element solvers, Tech. rep., Dassault Systémes Simulia Corp. (2011).
[48] M. Brun and A. Batti and A. Combescure and A. Gravouil, External coupling software based on macro-and micro-time scales for explicit/implicit multi-time-step co-computations in structural dynamics, Finite Elem. Anal. Des. 86 (2014) 101–119.